Journal of Applied Mechanics and Technical Physics, Vol. 45, No. 3, pp. 367–374, 2004

NUMERICAL SIMULATION OF A SUPERSONIC FLOW WITH TRANSVERSE INJECTION OF JETS

A. O. Beketaeva and A. Zh. Naimanova

UDC 532.526

A plane supersonic flow with symmetric perpendicular injection of jets through slots in the walls is numerically simulated with the use of Navier–Stokes equations. The effect of the jet pressure ratio and Mach number on the flow structure is considered. The angle of inclination of the shock wave and the separation-region length are found as functions of the jet pressure ratio. The influence of the jet pressure ratio on the increase in the lift force arising owing to interaction of the flow with the injected jet is found.

Key words: *supersonic flow, jet injection, Navier–Stokes equations.*

Introduction. Injection of a transverse jet into a supersonic flow generates a lift force normal to the surface of the flying vehicle. The use of this force for flow control is attractive because of its effectiveness and fast response at an arbitrary flight altitude. It follows from physical considerations that the interaction force depends on the parameters of the injected jet.

The flow around jets and obstacles has been comprehensively considered in experiments [1–4]. Among theoretical works, the papers with numerical simulation of transverse injection of hydrogen in the duct of an air-breathing engine should be mentioned [5–7]. These papers, however, describe mainly test computations and do not involve numerical simulations of the effect of some parameters of practical importance, such as the Mach number, slot width, and jet pressure ratio, on the flow structure. The reason is the complicated character of the flow in the injection region: there are separation regions both ahead of the jet and behind it. In this case, full Navier–Stokes equations should be used.

In the present paper, we consider a plane supersonic flow with perpendicular injection of jets from slots located symmetrically on the lower and upper walls of the channel. For convenience of computations, jet injection from the lower wall only is considered. The flow pattern is shown in Fig. 1.

Formulation of the Problem. The initial system consists of two-dimensional Navier–Stokes equations for a turbulent compressible gas flow, which is written in the Cartesian coordinate system in a conservative form:

$$\frac{\partial \boldsymbol{U}}{\partial t} + \frac{\partial \boldsymbol{E}(\boldsymbol{U})}{\partial x} + \frac{\partial \boldsymbol{F}(\boldsymbol{U})}{\partial z} = \frac{\partial \boldsymbol{V}_1(\boldsymbol{U}, \boldsymbol{U}_x)}{\partial x} + \frac{\partial \boldsymbol{V}_2(\boldsymbol{U}, \boldsymbol{U}_z)}{\partial x} + \frac{\partial \boldsymbol{W}_1(\boldsymbol{U}, \boldsymbol{U}_x)}{\partial z} + \frac{\partial \boldsymbol{W}_2(\boldsymbol{U}, \boldsymbol{U}_z)}{\partial z}, \tag{1}$$

$$\boldsymbol{U} = \begin{bmatrix} \rho \\ \rho u \\ \rho w \\ E_t \end{bmatrix}, \qquad \boldsymbol{E} = \begin{bmatrix} \rho u \\ \rho u^2 + P \\ \rho uw \\ (E_t + P)u \end{bmatrix}, \qquad \boldsymbol{F} = \begin{bmatrix} \rho w \\ \rho uw \\ \rho w^2 + P \\ (E_t + P)w \end{bmatrix},$$

Institute of Mathematics at the Ministry of Education and Science, Kazakhstan, Almaty 480100. Translated from Prikladnaya Mekhanika i Tekhnicheskaya Fizika, Vol. 45, No. 3, pp. 72–80, May–June, 2004. Original article submitted April 3, 2003; revision submitted September 8, 2003.

0021-8944/04/4503-0367

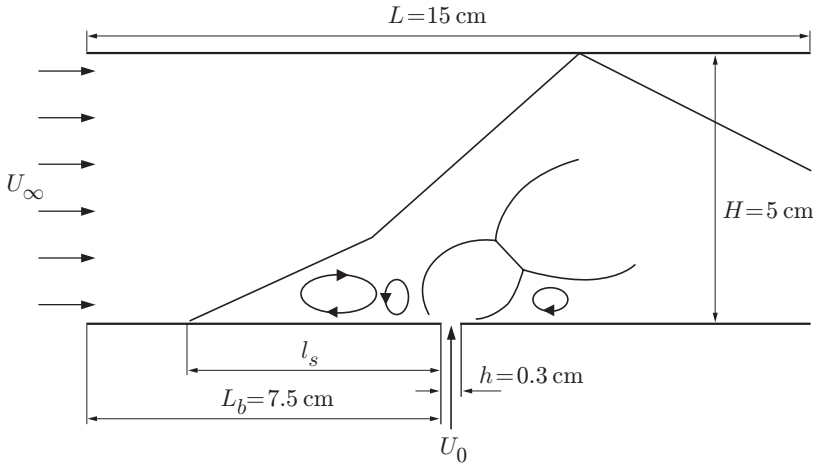

Fig. 1. Flow pattern.

$$\boldsymbol{V}_1 = \frac{1}{\mathrm{Re}}\begin{bmatrix} 0 \\ \dfrac{4}{3}\,\mu_t\,\dfrac{\partial u}{\partial x} \\ \mu_t\,\dfrac{\partial w}{\partial x} \\ \mu_t w\,\dfrac{\partial w}{\partial x} + \dfrac{4}{3}\,\mu_t u\,\dfrac{\partial u}{\partial x} + \dfrac{\mu_t}{(\gamma-1)\mathrm{M}_\infty^2\mathrm{Pr}}\,\dfrac{\partial T}{\partial x} \end{bmatrix}, \quad \boldsymbol{V}_2 = \frac{1}{\mathrm{Re}}\begin{bmatrix} 0 \\ -\dfrac{2}{3}\,\mu_t\,\dfrac{\partial w}{\partial z} \\ \mu_t\,\dfrac{\partial u}{\partial z} \\ \mu_t w\,\dfrac{\partial u}{\partial z} - \dfrac{2}{3}\,\mu_t u\,\dfrac{\partial w}{\partial z} \end{bmatrix},$$

$$\boldsymbol{W}_1 = \frac{1}{\mathrm{Re}}\begin{bmatrix} 0 \\ \mu_t\,\dfrac{\partial w}{\partial x} \\ -\dfrac{2}{3}\,\mu_t\,\dfrac{\partial u}{\partial x} \\ \mu_t u\,\dfrac{\partial w}{\partial x} - \dfrac{2}{3}\,\mu_t w\,\dfrac{\partial u}{\partial x} \end{bmatrix}, \quad \boldsymbol{W}_2 = \frac{1}{\mathrm{Re}}\begin{bmatrix} 0 \\ \mu_t\,\dfrac{\partial u}{\partial z} \\ \dfrac{4}{3}\,\mu_t\,\dfrac{\partial w}{\partial z} \\ \mu_t u\,\dfrac{\partial u}{\partial z} + \dfrac{4}{3}\,\mu_t w\,\dfrac{\partial w}{\partial z} + \dfrac{\mu_t}{(\gamma-1)\mathrm{M}_\infty^2\mathrm{Pr}}\,\dfrac{\partial T}{\partial z} \end{bmatrix},$$

$$P = (\gamma-1)\Big(E_t - \rho\,\frac{u^2+w^2}{2}\Big), \quad T = \frac{1}{\rho c_v}\Big(E_t - \rho\,\frac{u^2+w^2}{2}\Big), \quad c_v = \frac{1}{\gamma(\gamma-1)\mathrm{M}_\infty^2}.$$

Here, u and w are the components of flow velocity in the longitudinal and transverse directions, ρ is the density, P is the pressure, T is the temperature, E is the energy, c_v is the specific heat at constant volume, γ is the ratio of specific heats, M_0 and M_∞ are the jet and flow Mach numbers, μ_t is the turbulent viscosity, Re is the Reynolds number, and Pr is the Prandtl number; the subscripts ∞ and 0 refer to the flow and jet parameters, respectively.

The initial system (1) is written in a dimensionless form. The governing parameters are the parameters at the entrance (u_∞, ρ_∞, and T_∞), the pressure and total energy are normalized to $\rho_\infty u_\infty^2$, and the reference length is the slot width.

System (1) is closed by the Baldwin–Lomax algebraic model of turbulence [8].

The boundary conditions have the following form:

— at the entrance ($x = 0$, $0 \leqslant z \leqslant H$),

$$u = 1, \qquad w = 0, \qquad \rho = 1, \qquad T = 1;$$

— on the lower wall ($z = 0$, $0 < x \leqslant L$),

$$u = 0, \qquad w = 0, \qquad \frac{\partial T}{\partial z} = 0,$$

— on the slot ($z = 0$, $L_b \leqslant x \leqslant L_b + h$),

$$u = 0, \qquad T = 0.6, \qquad w = \sqrt{T}\,\mathrm{M}_0/\mathrm{M}_\infty, \qquad P_0 = nP_\infty$$

($n = P_0/P_\infty$ is the jet pressure ratio, P_0 is the jet pressure, and P_∞ is the flow pressure);

— a boundary layer on the wall is set in the input section, and the profile of longitudinal velocity is approximated by a power law [9];

— the following condition of symmetry is imposed on the upper wall ($z = H$, $0 < x \leqslant L$):

$$w = 0, \qquad \frac{\partial u}{\partial z} = 0, \qquad \frac{\partial \rho}{\partial z} = 0, \qquad \frac{\partial T}{\partial z} = 0$$

— nonreflecting conditions are set at the exit [10].

Method of the Solution. To take into account the flow in the boundary layer, near the wall, and near the slot, i.e., in regions of high gradients, more accurately, we refine the grid in the longitudinal and transverse directions by the transformations

$$\xi = \xi(x), \qquad \eta = \eta(z). \tag{2}$$

Equations (1) acquire the following form in the generalized coordinates:

$$\frac{\partial \tilde{\boldsymbol{U}}}{\partial t} + \frac{\partial \tilde{\boldsymbol{E}}}{\partial \xi} + \frac{\partial \tilde{\boldsymbol{F}}}{\partial \eta} = \frac{\partial \tilde{\boldsymbol{V}}_1}{\partial \xi} + \frac{\partial \tilde{\boldsymbol{V}}_2}{\partial \xi} + \frac{\partial \tilde{\boldsymbol{W}}_1}{\partial \eta} + \frac{\partial \tilde{\boldsymbol{W}}_2}{\partial \eta}. \tag{3}$$

Here, $\tilde{\boldsymbol{U}} = J^{-1}\boldsymbol{U}$, $\tilde{\boldsymbol{E}} = \xi_x J^{-1}\boldsymbol{E}$, $\tilde{\boldsymbol{F}} = \eta_z J^{-1}\boldsymbol{F}$, $\tilde{\boldsymbol{V}}_1 = \xi_x J^{-1}\boldsymbol{V}_1$, $\tilde{\boldsymbol{V}}_2 = \xi_x J^{-1}\boldsymbol{V}_2$, $\tilde{\boldsymbol{W}}_1 = \eta_z J^{-1}\boldsymbol{W}_1$, $\tilde{\boldsymbol{W}}_2 = \eta_z J^{-1}\boldsymbol{W}_2$, and $J = \partial(\xi, \eta)/\partial(x, z)$ is the Jacobian of mapping.

In what follows, the tilde is omitted for convenience.

System (3) linearized with respect to the vector $\boldsymbol{U}$ is solved by the Beam–Warming method:

$$\boldsymbol{U}^{n+1} + \Delta t\Big(\frac{\partial \boldsymbol{E}^{n+1}}{\partial \xi} + \frac{\partial \boldsymbol{F}^{n+1}}{\partial \eta} - \frac{\partial \boldsymbol{V}_1^{n+1}}{\partial \xi} - \frac{\partial \boldsymbol{V}_2^{n+1}}{\partial \xi} - \frac{\partial \boldsymbol{W}_1^{n+1}}{\partial \eta} - \frac{\partial \boldsymbol{W}_2^{n+1}}{\partial \eta}\Big) = \boldsymbol{U}^n + O(\Delta t^2). \tag{4}$$

Here,

$$\boldsymbol{E}^{n+1} \approx A^n \boldsymbol{U}^{n+1}, \qquad \boldsymbol{F}^{n+1} \approx B^n \boldsymbol{U}^{n+1}; \tag{5}$$

$A = \partial \boldsymbol{E}/\partial \boldsymbol{U}$ and $B = \partial \boldsymbol{F}/\partial \boldsymbol{U}$ are the Jacobian matrices [12].

The terms containing the second derivatives are presented as sums of two vectors

$$\boldsymbol{V}_1^{n+1} = \boldsymbol{V}_{11}^{n+1} + \boldsymbol{V}_{12}^n, \qquad \boldsymbol{W}_2^{n+1} = \boldsymbol{W}_{21}^{n+1} + \boldsymbol{W}_{22}^n, \tag{6}$$

where

$$\boldsymbol{V}_{11}^{n+1} = \frac{\mu_t \xi_x}{\mathrm{Re}\, J}\Big[0, \frac{4}{3}\frac{\partial}{\partial \xi}\Big(\frac{u\rho}{\rho}\Big)^{n+1}, \frac{\partial}{\partial \xi}\Big(\frac{w\rho}{\rho}\Big)^{n+1}, \frac{\gamma}{\mathrm{Pr}}\frac{\partial}{\partial \xi}\Big(\frac{E_t}{\rho}\Big)^{n+1}\Big]^{\mathrm{t}},$$

$$\boldsymbol{W}_{21}^{n+1} = \frac{\mu_t \eta_z}{\mathrm{Re}\, J}\Big[0, \frac{\partial}{\partial \eta}\Big(\frac{u\rho}{\rho}\Big)^{n+1}, \frac{4}{3}\frac{\partial}{\partial \eta}\Big(\frac{w\rho}{\rho}\Big)^{n+1}, \frac{\gamma}{\mathrm{Pr}}\frac{\partial}{\partial \eta}\Big(\frac{E_t}{\rho}\Big)^{n+1}\Big]^{\mathrm{t}},$$

and the vectors $\boldsymbol{V}_{12}^n$ and $\boldsymbol{W}_{22}^n$ contain the remaining dissipative functions of the form

$$\boldsymbol{V}_{12}^n = \frac{\xi_x^2}{\mathrm{Re}\, J}\Big[0, 0, 0, \Big[\Big(\mu_t - \frac{\gamma \mu_t}{\mathrm{Pr}}\Big)\Big(w\frac{\partial w}{\partial \xi}\Big) + \Big(\frac{4}{3}\mu_t - \frac{\gamma \mu_t}{\mathrm{Pr}}\Big)u\frac{\partial u}{\partial \xi}\Big]^n\Big]^{\mathrm{t}},$$

$$\boldsymbol{W}_{22}^n = \frac{\eta_z^2}{\mathrm{Re}\, J}\Big[0, 0, 0, \Big[\Big(\mu_t - \frac{\gamma \mu_t}{\mathrm{Pr}}\Big)\Big(u\frac{\partial u}{\partial \eta}\Big) + \Big(\frac{4}{3}\mu_t - \frac{\gamma \mu_t}{\mathrm{Pr}}\Big)w\frac{\partial w}{\partial \eta}\Big]^n\Big]^{\mathrm{t}}.$$

For flux vectors with mixed derivatives, we use explicit approximation with a uniform time step:

$$\boldsymbol{V}_2^{n+1} = 2\boldsymbol{V}_2^n - \boldsymbol{V}_2^{n-1} + O(\Delta t^2), \qquad \boldsymbol{W}_1^{n+1} = 2\boldsymbol{W}_1^n - \boldsymbol{W}_1^{n-1} + O(\Delta t^2). \tag{7}$$

With allowance for (5)–(7), system (4) becomes

$$\Big[I+\Delta t\Big\{\frac{\partial A^n}{\partial\xi}+\frac{\partial B^n}{\partial\eta}-\frac{\partial}{\partial\xi}\,\frac{\mu_t\xi_x^2}{\mathrm{Re}\,J}\,\frac{\partial}{\partial\xi}\Big(\frac{1}{\boldsymbol{U}_1^n}\Big)-\frac{\partial}{\partial\eta}\,\frac{\mu_t\eta_z^2}{\mathrm{Re}\,J}\,\frac{\partial}{\partial\eta}\Big(\frac{1}{\boldsymbol{U}_1^n}\Big)\Big\}\Big]\boldsymbol{U}^{n+1}$$

$$=\boldsymbol{U}^n+\Delta t\Big[2\Big(\frac{\partial\boldsymbol{V}_2^n}{\partial\xi}+\frac{\partial\boldsymbol{W}_1^n}{\partial\eta}\Big)-\Big(\frac{\partial\boldsymbol{V}_2^{n-1}}{\partial\xi}+\frac{\partial\boldsymbol{W}_1^{n-1}}{\partial\eta}\Big)+\frac{\partial\boldsymbol{V}_{12}^n}{\partial\xi}+\frac{\partial\boldsymbol{W}_{22}^n}{\partial\eta}\Big]+O(\Delta t^2). \tag{8}$$

Applying factorization to (8), we obtain two one-dimensional operators, which are resolved by matrix sweep:

$$\begin{aligned}&\text{Step 1:}\quad \Big[I+\Delta t\Big\{\frac{\partial A^n}{\partial\xi}-\frac{\partial}{\partial\xi}\,\frac{\mu_t\xi_x^2}{\mathrm{Re}\,J}\,\frac{\partial}{\partial\xi}\Big(\frac{1}{\boldsymbol{U}_1^n}\Big)\Big\}\Big]\boldsymbol{U}^*=RHS^n,\\ &\text{Step 2:}\quad \Big[I+\Delta t\Big\{\frac{\partial B^n}{\partial\eta}-\frac{\partial}{\partial\eta}\,\frac{\mu_t\eta_z^2}{\mathrm{Re}\,J}\,\frac{\partial}{\partial\eta}\Big(\frac{1}{\boldsymbol{U}_1^n}\Big)\Big\}\Big]\boldsymbol{U}^{n+1}=\boldsymbol{U}^*\end{aligned} \tag{9}$$

[RHS^n is the right side of Eq. (8)].

In approximation of derivatives in convective and diffusion terms, we use second-order central-difference operators.

Analysis of Results. The parameters of coordinate transformation (2) have the form [12]

$$\xi=K+\frac{1}{\tau}\,\mathrm{arcsinh}\,\Big[\Big(\frac{x}{x_c}-1\Big)\sinh\,(\tau K)\Big],\qquad \eta=H\Big[(\beta+1)-(\beta-1)\Big(\frac{\beta+1}{\beta-1}\Big)^{1-z/a}\Big]\Big/\Big[\Big(\frac{\beta+1}{\beta-1}\Big)^{1-z/a}+1\Big],$$

where

$$K=\frac{1}{2\tau}\ln\frac{1+(\mathrm{e}^{\tau}-1)x_c/L}{1-(\mathrm{e}^{\tau}-1)x_c/L},$$

β and τ are refinement factors ($\beta>1$ and $\tau>1$), a is the height of the computational domain in the generalized coordinates, and x_c is the point with respect to which grid refinement is performed. To suppress high-frequency disturbances, second-order smoothing with a small coefficient ε at smoothing terms was introduced into solution (9). The computation was performed on a 101×61 space grid with respect to spatial coordinates.

To test the numerical method, we first computed a test problem: perpendicular injection of a gas with the parameters $\mathrm{M}_0=1$, $T=217$ K, and $P=1.24$ MPa through a slot 0.0559 cm wide into an air flow with $\mathrm{M}_\infty=2.9$, $T=108$ K, and $P=0.0663$ MPa in a rectangular-section channel. The channel height and length were 7.62 and 15 cm, respectively. The slot was located at a distance of 10 cm from the input section. The results of the numerical experiment were in satisfactory agreement with experimental data and numerical calculations of other authors [5, 6].

Figures 2–6 show the results of numerical calculations of the problem with the parameters $\mathrm{M}_\infty=4$, $\mathrm{M}_0=1$, $\mathrm{Pr}=0.9$, $\mathrm{Re}=10^4$, and $\gamma=1.4$.

The distributions of isobars for two values of the jet pressure ratio are shown in Fig. 2. Because of deceleration of the incoming flow, the pressure ahead of the jet increases, and a bow shock wave (indicated by 1 in Fig. 2) is formed. An oblique shock wave 2 emanates upstream from the bow shock wave. In addition to the separation region, there is also a supersonic flow region behind the oblique shock wave; subsequent flow deceleration is accompanied by emergence of a second shock wave: barrel shock 3 parallel to the jet axis. It follows from Fig. 2 that the detached shock wave, oblique shock wave, and barrel shock wave intersect at one point to form a complicated λ-shaped structure of shock waves 4. The pressure along the front boundary of the jet is not constant. As it follows from the experiment of [3], this pressure is maximum in the region behind the triple point, in particular, behind the barrel shock wave. It is seen from the distributions of isobars that the pressure maximum ($P_{\max}=0.15$ in Fig. 2a and 0.24 in Fig. 2b) is located behind the lower part of the barrel shock wave.

An analysis of the influence of the jet pressure ratio on the bow shock wave shows that the angle of inclination of the latter increases with increasing pressure ratio behind the shock wave and ahead of it (cf. Figs. 2a and 2b). The effect of the jet pressure ratio on the angle of inclination of the bow shock wave is illustrated in Fig. 3 [$\alpha=\arctan\,(\max\,(w/u))$].

The velocity-vector field for two values of the jet pressure ratio is shown in Fig. 4. The zone adjacent to the wall contains two vortices formed as a result of primary and secondary separations of the flow from the wall

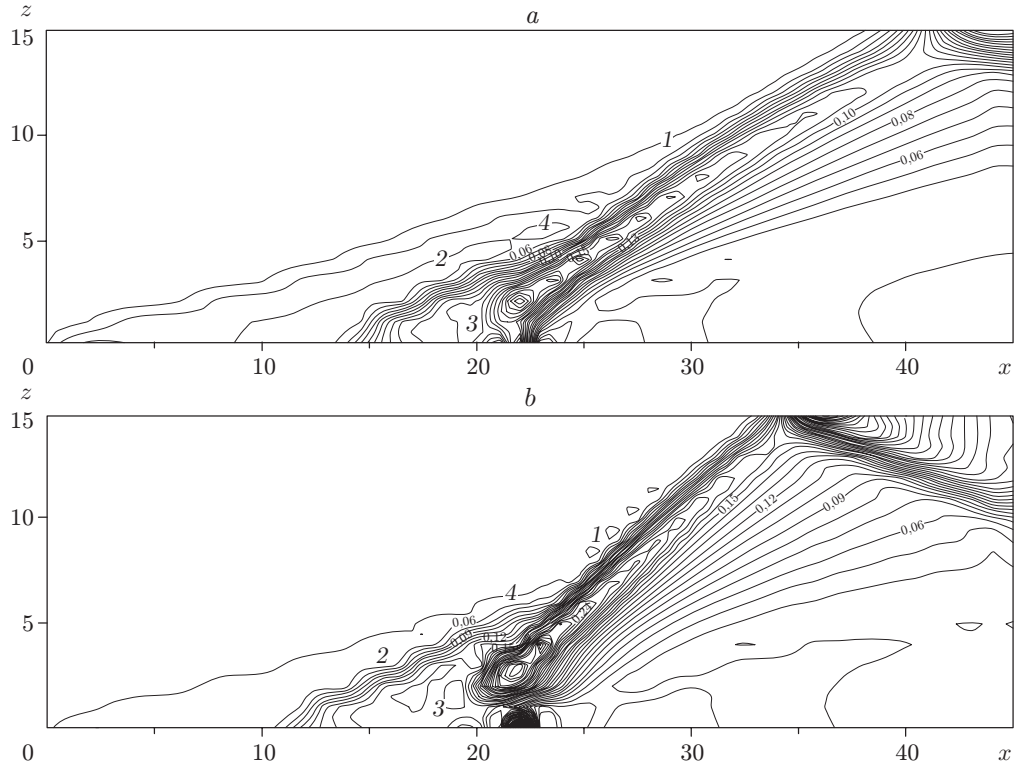

Fig. 2. Field of isobars for $n = 4$ (a) and 10 (b).

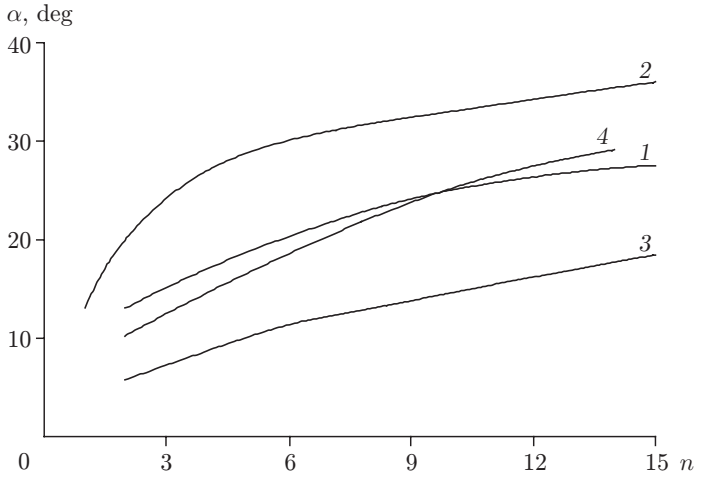

Fig. 3. Effect of the jet pressure ratio on the angle of inclination of the bow shock wave (curves 1 and 2) and reflected shock wave (curves 3 and 4): $M_0 = 1$ (1 and 3) and 2 (2 and 4).

upstream of the jet. The vortices rotate in the opposite directions because part of the air flow immediately near the wall passes through shock-wave portions, turns downward to the wall, penetrates into the separated-flow region, and spreads in the opposite directions. The vortex located closer to the jet moves anticlockwise, and the vortex located at a greater distance moves clockwise, which agrees with the experimental results of [1]. It is also well seen in Fig. 4 that the velocity vector deviates upward because of the presence of the oblique and bow shock waves, and this deviation increases with increasing jet pressure ratio, as it follows from the comparison of Figs. 4a and 4b. The vortex zone ahead of the jet is significantly greater than the separation region behind the jet. Apparently, boundary-layer separation ahead of the jet is conditioned by two factors: opposite pressure gradient and bow shock

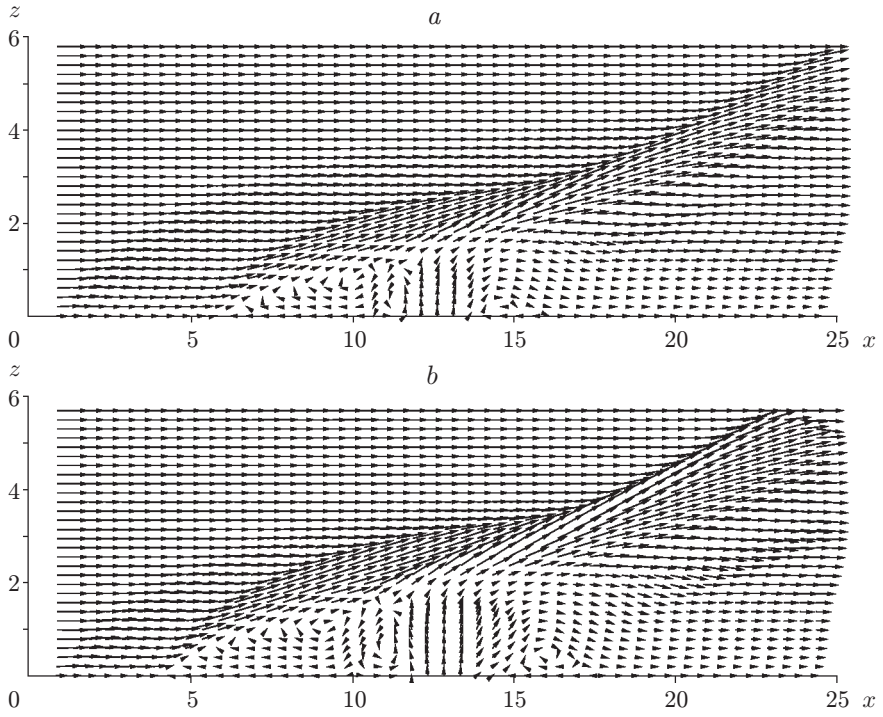

Fig. 4. Velocity-vector field for $n = 4$ (a) and 10 (b).

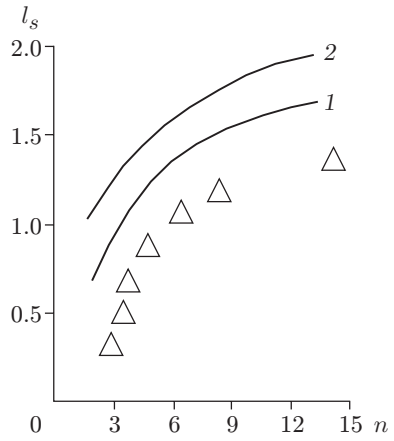

Fig. 5. Effect of the jet pressure ratio on the separation-region length for $M_\infty = 3$, Pr $= 0.9$, Re $= 1.87 \cdot 10^7$, $\gamma = 1.4$, and slot width of 14 mm: $M_0 = 1$ (1) and 1.5 (2); the point show the experimental results of [1].

wave–boundary layer interaction. The separation region behind the jet in a supersonic flow is additionally affected by the rarefaction zone [5]. For a jet pressure ratio $n = 10$ (Fig. 4b), the separation region ahead of the jet is much greater than for $n = 4$ (Fig. 4a), which also confirms the influence of the bow shock wave on vortex-zone formation.

A numerical analysis shows that the scheme of the flow around the jet is equivalent to the flow pattern around a cylinder whose diameter is equal to the slot width and which is mounted on the wall at a certain angle [4]. This similarity was established in the experiments of [2]. In the experiments of [1, 3], the normal shock was observed instead of the barrel shock. The reason is that the experiments of [1, 3] were performed with very high jet pressure ratios ($n = 50$–200).

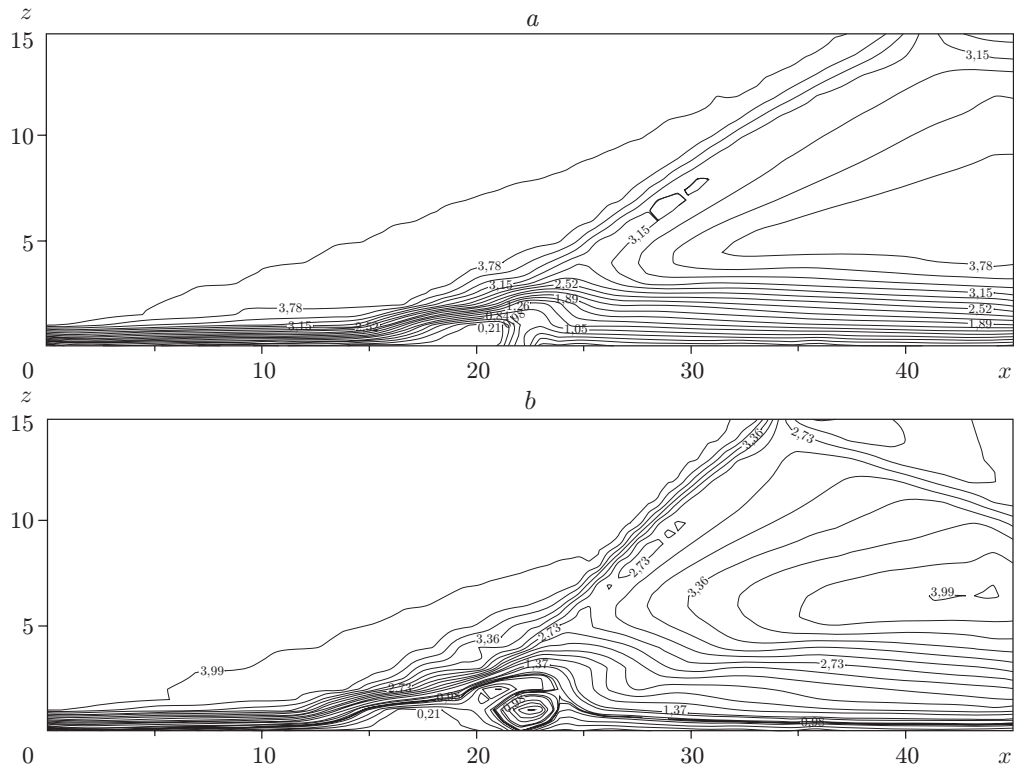

Fig. 6. Distribution of the local Mach number for $n = 4$ (a) and 10 (b).

The force of interaction is an integral of the product of excess pressure in the separation region and an area element. The lift force is determined from the pressure distribution on the wall by the formula

$$F = \int\limits_{l_s} (P - P_\infty)\, dl_s,$$

where l_s is the separation-region length. It follows from the calculation results that $F = 2.88$ and 4.03 for $n = 4$ and 10, respectively, i.e., a 2.5-fold increase in the jet pressure ratio leads to a 1.4-fold increase in the lift force.

The separation-region length versus the jet pressure ratio for $\mathrm{M}_\infty = 3$, $\mathrm{Pr} = 0.9$, $\mathrm{Re} = 1.87 \cdot 10^7$, and $\gamma = 1.4$ is compared with the experimental data of [1] in Fig. 5. It should be noted that the experiment corresponded to a three-dimensional case. The qualitative pattern for a two-dimensional case is similar to a three-dimensional case, but the values of l_s are higher, which is explained by the absence of lateral spillage.

The flow structure near the jet is illustrated in Fig. 6, which shows the distribution of the local Mach number $\mathrm{M} = \sqrt{u^2 + w^2}\,/c$ (c is the local velocity of sound). In the case with $n = 10$ (Fig. 6b), the jet entering the flow with a sonic velocity becomes supersonic at a certain distance because of the drastic acceleration immediately after injection; in this process, the Mach number increases to 1.9. Then, the boundary of the supersonic region is closed, forming a circle. Apparently, this circle corresponds to the barrel, which is a consequence of interaction of the system of shock waves separating supersonic and subsonic regions in the jet itself. A similar barrel was obtained in the numerical calculations of [7] with the Mach disk corresponding to the upper boundary of the barrel. The flow behind the barrel is decelerated and becomes subsonic with a Mach number $\mathrm{M} = 0.8$. Finally, the jet flow is accelerated and passes to a supersonic region, and the Mach numbers increase to $\mathrm{M} = 3$ and higher, which corresponds to the value of M in the main flow. A significant increase in the circle size is observed, depending on the jet pressure ratio. In particular, for the lower value $n = 4$ (Fig. 6a), the flow is not accelerated so sharply, and the Mach number inside the barrel increases to 1.2 only.

REFERENCES

1. A. I. Glagolev, A. I. Zubkov, and Yu. A. Panov, "Supersonic flow around a gaseous jet obstacle on a flat plate," *Izv. Akad. Nauk SSSR, Mekh. Zhidk. Gaza*, No. 3, 97–102 (1967).
2. V. S. Avduevskii, K. I. Medvedev, and M. N. Polyanskii, "Interaction of a supersonic flow with a transverse jet injected through a circular orifice in a flat plate," *Izv. Akad. Nauk SSSR, Mekh. Zhidk. Gaza*, No. 5, 193–197 (1970).
3. A. I. Glagolev, A. I. Zubkov, and Yu. A. Panov, "Interaction of a gas jet exhausting from an orifice in a flat plate with a supersonic flow," *Izv. Akad. Nauk SSSR, Mekh. Zhidk. Gaza*, No. 2, 99–102 (1968).
4. V. S. Avduevskii and K. I. Medvedev, "Physical features of the flow in the separation region upon three-dimensional shock wave–boundary layer interaction," *Izv. Akad. Nauk SSSR, Mekh. Zhidk. Gaza*, No. 1, 25–33 (1967).
5. J. S.Shuen and S. Yoon, *AIAA J.*, No. 12, 1752–1760 (1989).
6. E. H. Weidner and J. Ph. Drummond, "Numerical study of staged fuel injection," *AIAA J.*, **20**, No. 10, 1426–1431 (1982).
7. R. Ramakrishnan and D. J. Singh, "Modeling scramjet combustor flowfields with a grid adaptation scheme,"*AIAA J.*, **32**, No. 5, 930–935 (1994).
8. C. Fletcher, *Computational Techniques for Fluid Dynamics*, Springer-Verlag, Heidelberg (1988).
9. G. Schlichting, *Boundary Layer Theory*, McGraw-Hill, New York (1968).
10. K. W. Thompson, "Time dependent boundary conditions for hyperbolic systems," *J. Comput. Phys.*, **68**, No. 1, 1–24 (1987).
11. R. M. Beam and R. F. Warming, "An implicit factored scheme for the compressible Navier–Stokes equations," *AIAA J.*, **16**, 393–402 (1978).
12. D. Anderson, J. Tannehill, and R. Pletcher, *Computational Fluid Mechanics and Heat Transfer*, Hemisphere, New York (1984).
13. L. B. Schiff and J. L. Steger, "Numerical simulation of steady supersonic viscous flows," *AIAA J.*, **18**, 1421–1430 (1980).